Applied Clay Science 247 (2024) 107211

Contents lists available at ScienceDirect

Applied Clay Science

journal homepage: www.elsevier.com/locate/clay

Research Paper

Environmental significance of kaolinite variability over the last centuries in crater lake sediments from Central Mexico

Nathalie Fagel [a,*], Isabel Israde-Alcántara [b], Reza Safaierad [a], Marttiina Rantala [a], Sabine Schmidt [c], Gilles Lepoint [d], Pierre Pellenard [e], Nadine Mattielli [f], Sarah Metcalfe [g]

[a] AGEs, Department of Geology, Université de Liège, Belgium
[b] Instituto de Investigaciones en Ciencias de la Tierra, Universidad Michoacana de San Nicolás de Hidalgo, Morelia, Michoacán, Mexico
[c] Univ. Bordeaux, CNRS, Bordeaux INP, EPOC, UMR 5805, F-33600 Pessac, France
[d] LETIS, Université de Liège, Belgium
[e] Biogéosciences UMR 6282 CNRS/ub/EPHE, University of Burgundy, Dijon, France
[f] G-Time, Université Libre de Bruxelles, Belgium
[g] School of Geography, University of Nottingham, Nottingham NG7 2RD, United Kingdom

ARTICLE INFO

Keywords:
XRD mineralogy
XRF-core scanner
Runoff
Hydrolysis
Tropics
Late Holocene

ABSTRACT

Environmental conditions have a notable impact on clay minerals, primarily because of the chemical reactions they undergo with their immediate environment. These reactions are more pronounced in hot and humid tropical regions, and therefore, the study of clays deposited at the bottom of lakes in tropical regions can yield valuable insight into past environmental conditions. Here we present multiproxy records, including physical (magnetic susceptibility, grey-scale level and grain size), mineralogical (X-ray diffraction, Simultaneous Thermal Analysis, Fourier-Transform Infrared Spectroscopy), and geochemical (elemental composition by XRF-core scanner, organic geochemistry by IRMS) data, from three 210Pb-dated sediment cores (spanning recent centuries < 1470 CE) retrieved from crater lakes Los Espinos, Tacámbaro and Teremendo in the Trans-Mexican Volcanic Belt (TMVB), central Mexico. The mineralogical results showed that disordered kaolinite, formed by hydrolysis and hydrothermal alteration, was the predominant mineral in the sediments of the three lakes. The abundance of kaolinite changed in line with organic carbon and organic matter-related elements (Br, S and Ni) and showed opposite trends with lithogenic elements (Ti, K, and Fe). The geochemical data further suggested that increases in kaolinite abundance are linked to the formation of organo-mineral aggregates related to periods of elevated lake productivity that in turn may reflect lake level changes in the closed basins. In Lake Tacámbaro, following the construction of a canal in the early 20th century and subsequent regulation of lake level, the relationship between organic material and kaolinite was no longer present.

1. Introduction

Central Mexico (Fig. 1) is a suitable area to study climate variability as it lies beyond the northern limit of the Intertropical Convergence Zone (ITCZ) (Barron et al., 2012), and near the southern limit of the area influenced by the North American Monsoon (NAM) (Douglas et al., 1993; Higgins et al., 1999) which, together with convective storms, brings a summer dominated rainfall regime to the area. NAM rainfall is modulated by the El NiñoSouthern Oscillation (ENSO), with generally reduced/increased summer precipitation during El Niño/La Niña events (Castro et al., 2001). ENSO is a pseudo-periodic climate pattern involving variations in sea surface temperatures and winds over the eastern tropical Pacific (McPhaden et al., 2006).

The selected study area, i.e. the Trans Mexican Volcanic Belt (TMVB), has widespread crater lakes that are closed systems that may record climatic variability in their sedimentary sequences with relatively limited influence of direct human impact (Alcocer et al., 2000; Cobb et al., 2013). In crater lakes, the lake level is mainly controlled by the water balance between evaporation and precipitation (Gomez-Tagle Chavez et al., 2002). Direct anthropogenic perturbations in the TVMB with an impact on lake water level are recent. In fact, the sharp decrease in the water level of some lakes observed since the 1970s has been explained by the over-exploitation of groundwater for irrigation and urban purposes (Alcocer et al., 2000), which has led to the complete

* Corresponding author.
E-mail address: nathalie.fagel@uliege.be (N. Fagel).

https://doi.org/10.1016/j.clay.2023.107211
Received 23 August 2023; Received in revised form 31 October 2023; Accepted 6 November 2023
Available online 10 November 2023

drying of some crater lakes such as La Alberca in 2006 (Kienel et al., 2009) and la Hoya Rincon de Parangueo (Park et al., 2019).

In the TMVB area, previous paleolimnological studies have focused on deep (≥ 30 m) and/or large lakes with records of climate variability over the last 30 kyr (La Piscina de Yuriria) (Holmes et al., 2016) to 48 kyr (Pátzacuaro) (Bradbury, 2000). Additionally, only a limited number of laminated sediments with millennial and decadal resolution have been recovered. In Lake Tacámbaro, for example, a Holocene sequence (9.4 kyr BP to 1760 CE) is mainly laminated but the uppermost sediment (~190 yr) was lost during coring (Ortega-Guerrero et al., 2021). A centennial to decadal resolved paleoclimatic record for the last 6.7 kyr BP was retrieved from a partly laminated sedimentary sequence from the La Alberca maar lake (Wogau et al., 2019). Short cores from this lake and lake Hoya Rincón de Parangueo, both located in Valle de Santiago,

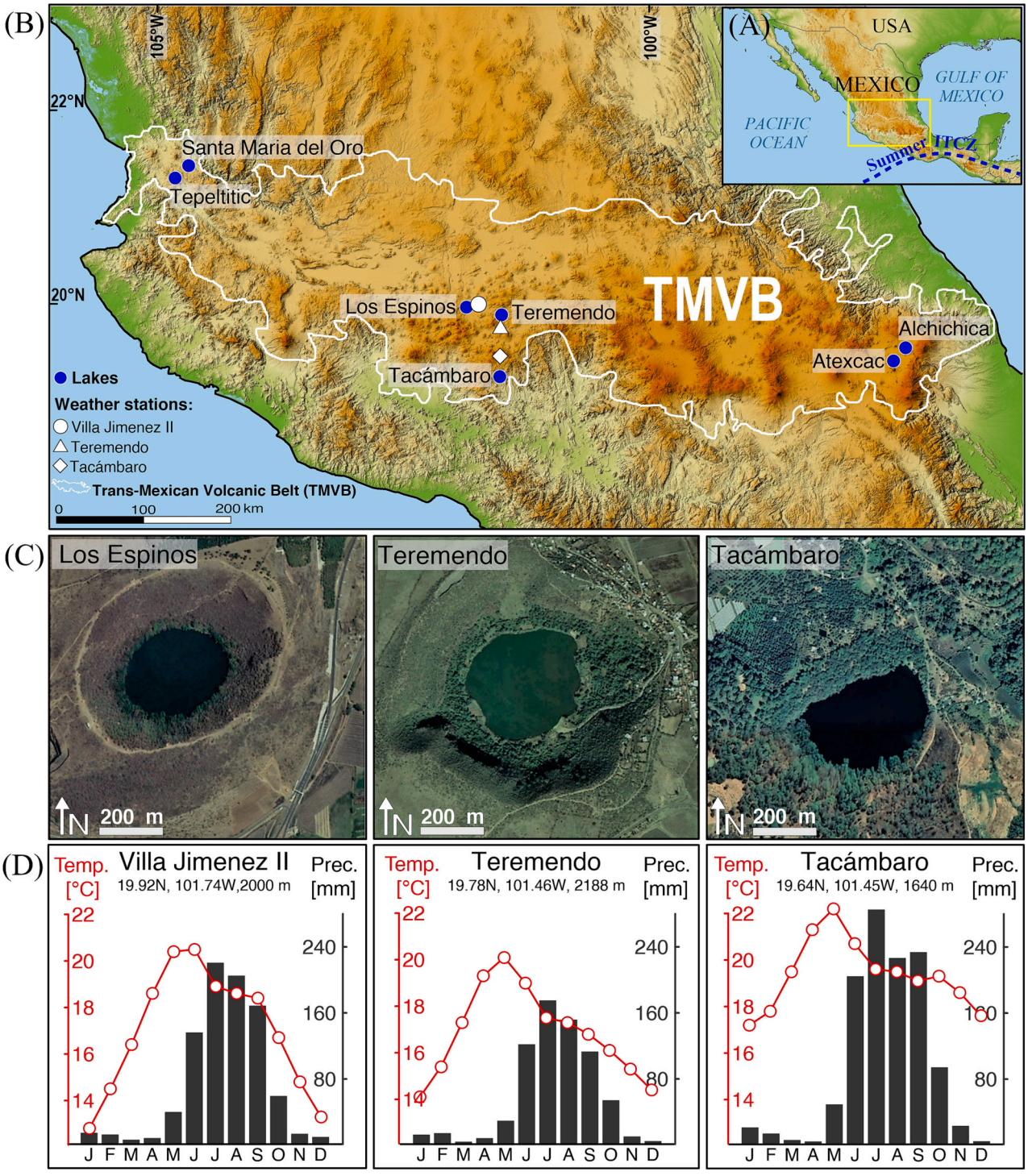

Fig. 1. (A) Regional map of North America with the location of the studied area (white square), i.e. the Trans-Mexican Volcanic Belt (TMVB) in Central Mexico, and the boreal summer position of the Inter-tropical Convergence Zone (ITCZ). (B) Enlarged map showing the location of the three studied crater lakes Los Espinos (LLEs), Tacámbaro (LTa) and Teremendo (LTe). (C) Photos of the three crater lakes (Google Earth image, 2022). (D) Climatographs of the meteorological stations located nearby the three crater lakes showing the monthly average temperature and precipitation data from 1981 to 2010 (Source: Servicio Meteorológico Nacional, Mexico, http://smn.cna.gob.mx/).

reveal varved sediments for the periods 1852–1973 and 1839–1943 CE, respectively (Kienel et al., 2009). These varved sediments consist of light coloured authigenic carbonate-rich laminae formed by a supersaturated water column during the dry season and dark-coloured detrital laminae formed by surface runoff during the wet season. Although some relationship was observed between detrital sedimentation and local precipitation, it was not significant (Kienel et al., 2009).

Lakes are sensitive sensors of environmental and climatic changes (e.g. Adrian et al., 2009), mainly influenced by seasonal temperature and precipitation regimes. In Central Mexico, the increase of temperature starting in spring (Fig. 1) favours stable stratification of the upper water column leading to a progressive nutrient limitation in summer, followed by water column mixing in winter (Winder et al., 2009). Such thermal control is manifested, for example, by changes in phytoplankton assemblages in Lake Tacámbaro (Caballero et al., 2016). Rainfall induces surface runoff which carries both organic and mineral detritus into the lake (Kienel et al., 2009). In tropical lakes, spring algal blooms are related to increased temperature, but also nutrients washed into the lake by rainfall (Lind et al., 1992). In summer, the intense rainfall increases water turbidity and dilutes nutrients in the stratified upper water column, leading to a reduction in biological productivity (Gomez-Tagle Chavez et al., 2002). Among other meteorological forcings, the impact of wind action on thermal stratification is limited in crater lakes due to their low surface/depth ratio and steep crater walls (Kienel et al., 2009; Briddon et al., 2023).

The mineralogy of crater lake sediments may be used as a reliable proxy for the degree of chemical weathering and physical erosion of the crater soil cover, which in turn reflects the climatic conditions within the closed watershed. Among the detrital minerals, clay minerals are formed in the upper soil profile by the weathering of parent rocks (Pedro, 1968; Singer, 1984; Warr, 2022). Their mineralogy reflects the degree of physical decomposition and chemical transformation during pedogenetic processes (Chamley, 1989; Weaver, 1989). Under a warm and humid tropical climate, the intense hydrolysis of primary minerals leads to a complete leaching of cations and partial removal of silica (i.e. monosialitisation process). The secondary clay mineral formed, i.e. kaolinite [$Al_2Si_2O_5(OH)_4$], is a combination of a layer of aluminium with a layer of silica (1:1 clay mineral). A stronger hydrolysis leads to a complete leaching of the silica and allows the formation of silica-free secondary phases such as gibbsite [$Al(OH)_3$], boehmite [AlO(OH)] or diaspore [AlOOH] in association with other immobile elements such as iron (Saalfeld and Wedde, 1974). In addition to climate, the topography and lithology of the parental rock also control clay formation (Singer, 1984). For instance, the volcanic rocks that constitute the parental rock of the crater flanks are more sensitive to weathering than other crystalline rocks. However, according to Chamley (1989), climate remains the most important influencing factor under strongly hydrolysing conditions.

The aim of this study is to compare mineralogical and geochemical proxies of three sedimentary cores retrieved from Central Mexico in order to explore the main environmental factors controlling the sedimentary cycle, from alteration processes and erosion to lacustrine sedimentation, over the past centuries. Particular emphasis is given to the evolution and significance of the relative abundance of kaolinite in the sedimentary records.

2. Study area

Sediment cores were collected from three crater lakes in the Michoacán-Guanajuato volcanic field, in central part of the TMVB (Fig. 1A and B). The TMVB is an active volcanic arc, located between ~18°30′N and 21°30′N, related to the oblique subduction of the Cocos Plate beneath the North American Plate (Ferrari et al., 2012). The studied lakes in the TMVB constitute promising sites for high-resolution paleolimnological studies (Fig. 1C). These lakes correspond to “maars” that originated by phreatomagmatic eruptions (Cifuentes and Fucugauchi, 1999) and range in altitude from 1475 to 2058 masl.

Based on meteorological data (30-year average: 1981–2010) from three stations near the lakes (Fig. 1D), the mean monthly temperature in Tacámbaro ranges from 17 to 22 °C (annual average 19 °C) while the temperatures are slightly cooler in Teremendo ($14 \leq T \leq 20$ °C) and Villa Jimenez (i.e. the station located 2 km NE of Lake Los Espinos, $13 \leq T \leq 21$ °C). >92% of the annual precipitation falls in summer, from late May to October (Fig. 1B). Tacámbaro is characterized by the highest mean annual precipitation of 1168 mm/yr. Teremendo is the driest location with 700 mm/yr, whereas Villa Jimenez station displays intermediate values with 896 mm/yr.

Los Espinos crater (19°54′25″ N, 101°46′06″ W, 1940 masl - Fig. 1C) is a well-preserved tuff volcanic cone located on the north-western margin of the Zacapu tectonic lacustrine basin (Hasenaka and Carmichael, 1985). Its formation dates back to 25 kyr BP. Its basement consists of basalts and andesites, which are hosted in granitic rocks (Sigala et al., 2017). The crater has an elliptical shape (0.33 km^2) with a NE-SW orientation and accommodates a lake of 350 m in diameter (area 0.1 km^2) with a maximum depth of 30 m (Siebe et al., 2012). The water column is mixed in winter (December–February) but stratified during the rest of the year (Hernández-Morales et al., 2011). The chlorophyll A ranges between 0.5 and 1.5 mg/m^3. The inner slopes of the crater are vegetated with tropical deciduous and gallery forests, helping to reduce the movement of sediments downslope into the lake.

The Tacámbaro crater (19°12′38″ N, 101°27′33″ W, 1475 masl - Fig. 1C) was formed during the Pliocene (Guilbaud et al., 2012). Its volcanic basement is made of basalts and dacites whereas the youngest <1 Ma volcanic rocks are andesite and basaltic andesites (Guilbaud et al., 2012). In this location, the host rocks are made of siliciclastic and carbonate rocks (Sigala et al., 2017). The crater is characterized by steep walls (28 m) and narrow shore zones, except on its eastern flank (Ortega-Guerrero et al., 2021). The lake is small with a diameter of 300 m (surface area 0.08 km^2) and a maximum depth of 28 m (Caballero et al., 2016; Sigala et al., 2017). The lake was a closed system until the construction of a canal at the beginning of the 20th century to regulate the lake depth (Ortega-Guerrero et al., 2021). The lake type is warm monomictic, yearly stratified except in January (Hernández-Morales, 2011). It is characterized by eutrophic conditions with annual maximum chlorophyll A concentrations ranging from 25 to 75 mg/m^3 (Sigala et al., 2017). The vegetation of the crater is diverse, ranging from a typical temperate forest to a low deciduous forest (Morales et al., 2008).

The Teremendo crater (0.65 km^2), formed during the Pliocene, has steep walls made of basalts and andesites overlying granitic basement (Soria-Caballero et al., 2019). The crater lake (19°48′25″ N, 101°27′15″ W, 2058 masl - Fig. 1C) is shallow (depth ≤ 9 m) (Sigala et al., 2017) and covers an area of 0.15 km^2 with a circular shape. The lake stratifies from March to November and is hypertrophic with an annual chlorophyll A concentration of ≥75 mg/m^3 (Sigala et al., 2017). Based on field observations, the crater is covered by a seasonal dry forest, which has been partially deforested and replaced by cattle pasture and shrubland. Additionally, the marginal areas of the lake are colonized by (semi-) aquatic plants.

3. Material and methods

3.1. Sedimentological analyses

In June 2019, three crater lakes in Central Mexico were sampled using a Uwitec® gravity corer, with a 9 cm core barrel. Cores were retrieved in the central part of each lake, namely LLEs19-2 (53 cm, water depth 30 m) from Lake Los Espinos, LTa19-3 (93.5 cm, water depth 26 m) from Lake Tacámbaro and LTe19-4 (109 cm, water depth 8 m) from Lake Teremendo (Fig. 1B & C). After the fieldtrip, the three cores were split lengthwise, described and photographed. Before transport, one half-core section was subsampled in one or two contiguous 4 cm wide rectangular plastic tubes ≤74 cm long for non-destructive analyses and

into 25 cm long x 4 cm wide x 1.5 cm deep aluminium boxes for destructive analyses. The second half-core section was stored at 4 °C for diatom and pollen analyses.

The subsamples within the plastic channels were scanned for physical (grayscale image, magnetic susceptibility) and X-ray Fluorescence (XRF) geochemical characterization of the sediment. Magnetic susceptibility (MS) of the sediment was measured at 5 mm intervals using a Bartington® instrument MS2E point sensor, following the protocol described in Bartington-Instruments (2008). Three measurements expressed in SI units, equivalent to 10^{-6} CGS, were averaged to obtain a representative profile (AGEs, Belgium). A SCOPIX X-ray image-processing system (EPOC, University of Bordeaux, France) was used at 58 kV, 10 mA and a step size of 15 μm to determine the grayscale image of the sediment cores (Migeon et al., 1998).

Wet bulk density was calculated by weighing 1 cm^3 of wet sediment at 1 cm intervals for the top 25 cm of the cores. Grain-size analyses were done with a sampling resolution of 4 to 5 cm using a Malvern® Mastersizer 2000 laser diffraction particle analyser (ARGENCO, University of Liège, Belgium). Each bulk sediment sample was dispersed in deionised water, sieved to 2 mm and introduced into the dispersion unit cell (Hydro 2000G). The sample volume was adjusted to reach a laser beam obscuration of 10 ± 5%. Before analysis, the sample was homogenised using a 2000 rpm stirrer and disaggregated using moderate ultrasonic waves (i.e. 2.6 W power). An average of three measurements was calculated for data reproducibility. The relative abundance of clay (i.e. <2 μm), silt (2–63 μm) and sand (>63 μm) fractions was calculated for each sample. The silt fraction was subdivided into fine (2–10 μm), medium (10–30 μm) and coarse silt (30–63 μm) fractions.

Mineralogical analysis was performed by X-ray diffraction (XRD) using a Bruker® D8-Advance Eco diffractometer (CuKα radiation, λ = 1.5418 Å, 40 kV, 25 mA) coupled with a Lynxeye XE detector (AGEs, University of Liège). The sampling resolution reaches up to 1 cm for LTa19-3 ($n = 72$) and 4 to 5 cm for LLEs19-3 ($n = 10$) and LTe19-4 ($n = 22$). The dried (40 °C) bulk sediment sample was ground by hand with an agate mortar. The powder was sieved at <150 μm and transferred to a plastic holder using the backside method (Moore and Reynolds, 1989) and scanned from 2 to 70° 2θ with a step size of 0.009°2θ and 0.5 s per step. Mineral identification and quantification were done using the EVA and TOPAS ® Bruker software, respectively. A Rietveld refinement was applied to all the minerals identified by XRD (Rietveld, 1967; Brindley, 1980b; Bish, 1993a; Środoń, 2002). Preferred orientations and unit cell parameters of the mineral phases were progressively adjusted to obtain a reconstructed XRD pattern as close as possible to the measured pattern.

To complement the XRD analysis, a Simultaneous Thermal Analyser (STA, Mettler-Toledo® STAR^e System) was used to follow the origin and transformation processes of the clay minerals through the sedimentary cycle. STA allows the degree of order-disorder of individual clay minerals to be estimated, giving clues on their origin and transformation processes (e.g. Patterson and Swaffield, 1987; Hemminger and Cammenga, 1989; Emmerich, 2010). Thermal analysis also provides information on the presence of disordered (Smykatz, 1974; Drits et al., 1995) and/or amorphous mineral phases, even at low abundances (Emmerich, 2010). The presence of these phases, which remain largely undetected in the XRD analysis, is indicative of mineral transformation and/or dissolution occurring in specific environmental conditions (e.g. pedogenesis, weathering). STA analysis was made on bulk sediment powder on a selection of 12 samples from the 3 cores characterized by variable proportions of kaolinite (AGEs, University of Liège). The sample weight loss (Thermogravimetric TG curve) and associated heat exchanges (Differential Scanning Calorimetry DSC curve) were followed at a constant heating rate of 20 °C per minute from 25 to 1200 °C under a nitrogen atmosphere (80 ml/min). The first derivative of the thermogravimetric curve (DTG) represents the rate of weight loss. It was calculated since DTG peak gives the specific temperatures characteristic of the different mineral components more accurately than the TG curve and indicates the characteristic temperature of the reactions occurring in the samples (Földvári, 2011), in particular dehydration and dehydroxylation for clay minerals. The STA data were processed using the evaluation software Metler Toledo STAR^e SW16.40.

Fourier Transform Infrared Spectroscopy (FTIR) was carried out on 8 samples already analyzed by STA using a Nicolet NEXUS Spectrometer (Laboratory of Mineralogy, University of Liège). Pellets were made from 2 mg of powdered sample, ground to <250 μm and 148 mg of potassium bromide. The measurement was made in the range of 4000 to 400 cm^{-1} with a resolution of 1 cm^{-1}. FTIR is a method commonly used to assess the degree of disorder (Lorentz et al., 2018).

Scanning Electron Microscope (SEM) imaging was carried out at the University of Burgundy (ARCEN analytical platform) on 6 samples using a Hitachi SU8230, with a resolution of 0.8 nm (15 kV, WD = 4 mm), equipped with a ThermoFisher Scientific UltraDry 30 mm^2 Energy Dispersive X-ray (EDS, 127 eV Mn energetic resolution) in order to comfort XRD and geochemical analyses. Sieved sediments at 30 μm were used for observations after aqueous suspension of the sediment on a SEM spinner covered with copper tape and hydrophilization under air plasma in primary vacuum.

An Avaatech XRF core scanner (EPOC, University of Bordeaux, France) equipped with a Fe—Mo tube was used with a step size of 1 mm to characterize the bulk sediment geochemistry (e.g. Frugone-Álvarez et al., 2017). Measurements of fourteen elements (i.e. Al, Si, S, K, Ca, Ti, Mn, Fe, Co, Ni, Br, Sr, Zr and Pb) were done with voltages of 10, 30 and 50 kV and counting times of 15, 20 and 25 s, respectively. Semi-quantitative concentration profiles of the elements were plotted through the depth of the sediment core based on the variation of their peak areas measured on XRF spectra and expressed as counts per second (cps). A statistical approach was applied to the XRF dataset using version 4.2.2 of the R environment (R Development Core Team, 2013). First, the XRF count data were transformed to centred log-ratio (clr) using *rgr* package (Garrett and Garrett, 2018). A Robust Principal Component Analysis (RPCA, Candès et al., 2011) was then applied to the clr data using the package *pcaPP* (Filzmoser et al., 2018) as proposed by Żarczyński et al. (2019). The 14 elements were included in the analysis. The principal components (PC) with an eigenvalue >1 were retained as significant for the total variance of the dataset (Davis, 2002).

Sediment organic geochemistry, including organic carbon (C) and nitrogen (N) stable isotope ratios ($\delta^{13}C$, $\delta^{15}N$) and elemental concentrations, was characterized by Isotope Ratio Mass Spectrometry (IRMS)/Elemental Analyser (EA) at LETIS (University of Liège, Belgium). The analysis was carried out at ~4 to 10 cm intervals using a VarioMicro Elementar analyser coupled to a precisION IRMS (LTe19-4). Prior to the analysis, the samples were acidified by exposing the freeze-dried and ground sediments to 37% HCl vapor for 10 h to remove carbonates. Bulk N was considered to comprise primarily organic nitrogen given the generally low concentration of inorganic nitrogen in lake sediments. For LTe19-4, the analysis was additionally carried out on non-acidified samples to evaluate the influence of acidification on elemental concentrations and isotope ratios. The patterns of acidified and non-acidified samples were consistent for all four variables ($R^2 > 0.94$) indicating that the trends are reliable. All values used in this study for the three lakes are from acidified samples. Variations in carbon and nitrogen isotope ratios are expressed using the delta-notation, i.e., as differences (‰) relative to international standards (VPDB for carbon, AIR for nitrogen). Precision of the $\delta^{13}C$ and $\delta^{15}N$ measurements based on repeat analyses were ± 0.27 and 0.97 SD, respectively. The carbon to nitrogen ratio (C/N) was calculated for each sample to estimate changes in the relative contribution of allochthonous and autochthonous organic matter (Meyers, 2003). C/N mass ratios were converted into atomic ratios by multiplying the values by 1.167.

3.2. Core chronology

The activities of ^{210}Pb, ^{226}Ra and ^{232}Th were measured on 1 cm thick samples in cores LLEs19-2, LTa19-3 and LTe19-4 with a low-background

and high-efficiency well-type gamma detector (EPOC, University of Bordeaux, France) until negligible excess ^{210}Pb was reached. The excess ^{210}Pb activities ($^{210}Pb_{xs}$) were calculated by subtracting the measured ^{226}Ra content from the total ^{210}Pb content. The Constant Flux/Constant Sedimentation model (CF/CS, Appleby and Oldfield, 1978) was applied to the $^{210}Pb_{xs}$ to calculate a mean sediment accumulation rate, which was used to estimate an age for each sediment layer.

4. Results

4.1. Sedimentology

Fig. 2 presents the SCOPIX image of the cores LLEs19-2 (Espinos), LTa19-3 (Tacámbaro) and LTe19-4 (Teremendo), along with the MS profiles and the abundance of clay (% <2 μm) and fine silt (% 2–10 μm) fractions (Table S1).

The sediment of LLEs19-2 was brownish dark (5YR 2/1, Munsell, 1975) with a fine organic-rich texture (average 24% organic matter), dominated by silt (78 ± 5%) and sand (20 ± 5%) with a small proportion of clay (2.6 ± 0.9%). Its MS profile ranged between 2.96 10^{-4} and 6.30 10^{-3} SI, with an average value of 1.55 10^{-3} SI. The MS displayed a few positive excursions between 10 and 15 cm, 33 to 35 cm and 49–51 cm, underlying darker and coarser multi-millimeter laminations. The highest sand fraction (29%) corresponded to the darker laminations at 14–15 cm. In the upper part of the SCOPIX image, a vertical burrow disturbed several mm-scale laminations observed between 4 and 7 cm. The lower part of the core (from 35 to 53 cm) was marked by abundant gastropod shells, especially between 35 and 43 cm.

The background colour of sediment core LTa19-3 was dusky brown (5YR 2/2) with several darker (brownish black 5 YR 2/2) multi-millimeter laminations (Munsell, 1975). A few shells were observed, especially in the lower core section (73–93.5 cm). The core was mainly composed of silt particles (80 ± 7%) associated with 20 ± 7% sand. The core section comprised between 39 and 52 cm was characterized by higher proportions of both clay (10 to 15%) and fine silt fractions (35 to 45%) than the core average (i.e. 5.5 ± 3% and 26 ± 8%, respectively). The LTa19-3 core displayed a similar range of MS variation from 3.48 10^{-4} to 6.310^{-3} SI as in the LLEs19-2 core but with a higher average value (2.03 10^{-3} SI). The MS values were low (0.8 10^{-3} SI) in the lower part of the core, increased up to 60 cm and then decreased irregularly from ~52 cm upwards. The organic matter content of the LTa19-3 core was on average 20% and reached up to 25% in the lower core section (60–93.5 cm).

The sediment in core LTe19-4 was brownish dark (5YR 2/1, Munsell, 1975) with a fine organic-rich texture (average 23% organic matter). The sediment was composed of silt (77 ± 8%) and sand grains (23 ± 8%) with a low proportion of clay particles (3.4 ± 1%). The sediment texture comprised mm-scale darker laminations between 95 and 49 cm and was more homogeneous in the upper 49 cm. The MS profile of core LTe19-4 ranged from 2.37 10^{-4} to 2.51 10^{-3} SI. The MS displayed a minimum value between 103.5 and 100 cm, in an interval containing the highest sandy fraction of the core (45% at 100–101 cm). MS fluctuated between 93.5 and 49 with 4 distinct peaks, also visible in the SCOPIX image, at 93.5, 61, 54.5 and 49.5 cm, followed by a decline from 49 cm upwards.

4.2. Mineralogy

Andesite (i.e. plagioclase) and kaolinite were the two main minerals identified in the three studied sediment cores, associated with diopside (i.e. pyroxene), hornblende (i.e. amphibole) and/or forsterite (i.e. olivine) and quartz (Table S2). Carbonate minerals, ubiquitous in LLEs19-2 (except at 14–15 cm) and in LTe19-4, were represented by calcite, aragonite and/or dolomite. In contrast, carbonate minerals were absent from Tacámbaro. In addition, accessory minerals such as oxides (i.e. hematite, magnetite) or sulphide (pyrite) were detected in some samples. The diffraction band observed between 20 and 30° 2θ revealed the presence of amorphous sedimentary components such as biogenic silica, organic matter or volcanic glass (e.g. Fagel et al., 2017).

In LLEs19-2 (Table S2a), andesite was the most abundant mineral (43% ±12) followed by kaolinite (33% ±8). The secondary phases were diopside (7% ±2.3), calcite (6.6% ±4.5) and aragonite (4.6% ±2.8). Quartz was present in trace amounts (1–3%) in all samples. Forsterite (2–6%) and hornblende (1–2%) were present in trace amounts. In addition to kaolinite, the phyllosilicates were also represented by traces of talc (≤ 1%), observed in a few samples.

With a core mean of 58% ±8, the relative abundance of kaolinite in LTa19-3 was higher than in LLEs19-2 with a range of variation between 37 and 76%. Traces of diaspore (0–2%) were suspected in the upper 60 cm core section whereas its abundance was slightly higher in the lower core section (3–6% - Table S2b). Andesite was the second most abundant mineral (24% ±5) in LTa19-3. Cristobalite represented an average abundance of 10% ± 3. Hornblende (<3%) and diopside (<1%) were present in low abundance in most samples. Quartz and hematite were ubiquitous whereas magnetite was identified in trace amounts (≤2%) in some samples. Traces of forsterite or talc were observed in only one sample. To get an overview of the mineral composition in LTa19-3 some XRD patterns are reported by core depth in Fig. S1. With the exception of talc and hornblende, which were found in only one sample, most minerals were detected in all samples, but at variable intensities quantified by Topas. As an example, Fig. S2 compares the raw XRD spectra of sample LTa19–3 15–16 cm with the Topas-derived reconstructed profile. For kaolinite, in particular, the unit cell parameters were modified from the structure given by Bish (1993b). A Rietveld refinement was first obtained by imposing two planes of preferential orientation (i.e. 001 and 100) and then by adjusting the unit cell parameters (a, b, c, α, β and γ). The cif file obtained is reported in the supplementary material (Text S1a).

Kaolinite (52% ±6) was the dominant mineral observed in LTe19-4, ranging from 41% at 54–55 cm to 65% at 100–101 cm. Kaolinite was followed by andesite (38% ±4). The other magmatic minerals (i.e. diopside, forsterite and hornblende) were only observed in one or two samples (Table S2c). Traces of cristobalite (<2%) were only detected in the upper samples (0–11 cm). Calcite (3.7% ±2) was present in low abundance in all samples, except in the uppermost (0–1 cm). Quartz (2.7% ±0.7) was ubiquitous. Dolomite and hematite were detected in traces in most samples.

In the three sediment cores, kaolinite was the unique clay mineral evidenced by a large reflection at 7.3 Å in the bulk mineralogy of all samples (Fig. S1), confirmed by SEM observation (Fig. S3). The TG curves displayed at least 2 main peaks between 50 and 130 °C and 400–500 °C corresponding to 5–7% and 8–12% of mass loss, respectively (Fig. 3). The DTG curves specified the temperature of these endothermic reactions, i.e. 73–98 °C and 444–474 °C respectively. A third exothermic peak was observed at 890–990 °C associated with a mass loss of ~3–5%. After heating up to 1200 °C the total weight loss averaged 20–33% of the original sample weight.

The FTIR analyses were done on two or three samples per core, those samples being characterized by a range of abundance in kaolinite (i.e. 27 to 41% in LLEs19-2; 59 to 76% in LTa19-3; 50 to 59% in LTe19-4). The samples from Tacámbaro and Teremendo displayed similar FTIR spectra with two absorption bands in the 3690–3620 cm^{-1} region and several bands over 1000 and 500 cm^{-1}. Note the first two adsorption bands near 3700–3600 cm^{-1} were not detected in the two samples from LLEs19–2 that were characterized by the lowest abundance of kaolinite in the bulk sediment.

4.3. Sediment geochemistry

XRF element profiles, SCOPIX curves, clay abundance and organic geochemistry of the three cores are plotted against core depth in Fig. 5. For LLEs19–2, Ti covaried inversely with the SCOPIX greyscale level (Fig. 5) whereas Br mimicked the SCOPIX curve. The darker sediment

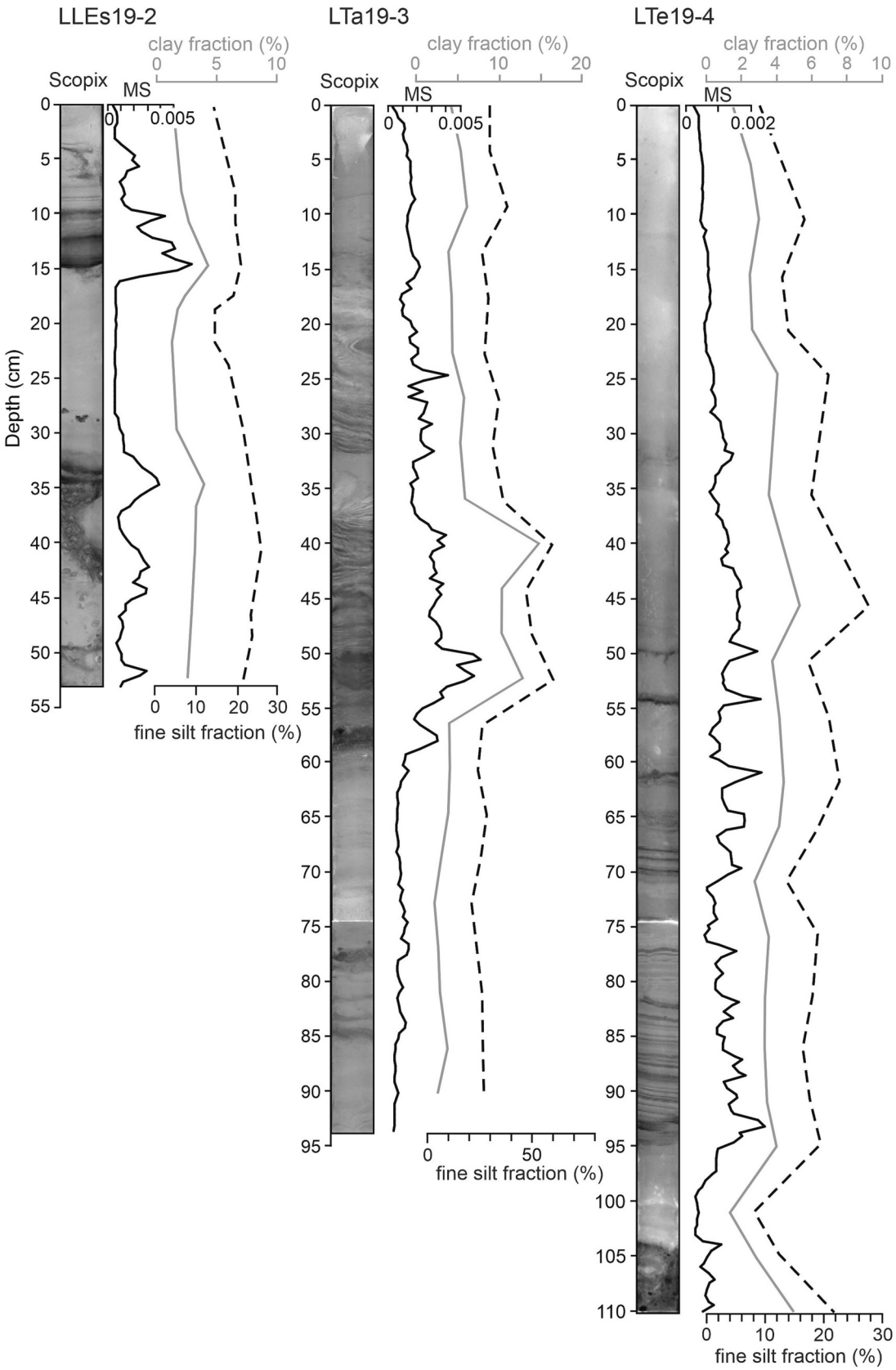

Fig. 2. Lithology of cores LLEs19-2, LTa19-3 and LTe19-4. SCOPIX high-resolution image of the core, magnetic susceptibility profiles (plain black line) and abundance of clay (% <2 μm - upper axis, grey plain line) and fine silt (% 2–10 μm - lower axis, black dashed line) fraction. Grain-size data are reported in Table SM1.

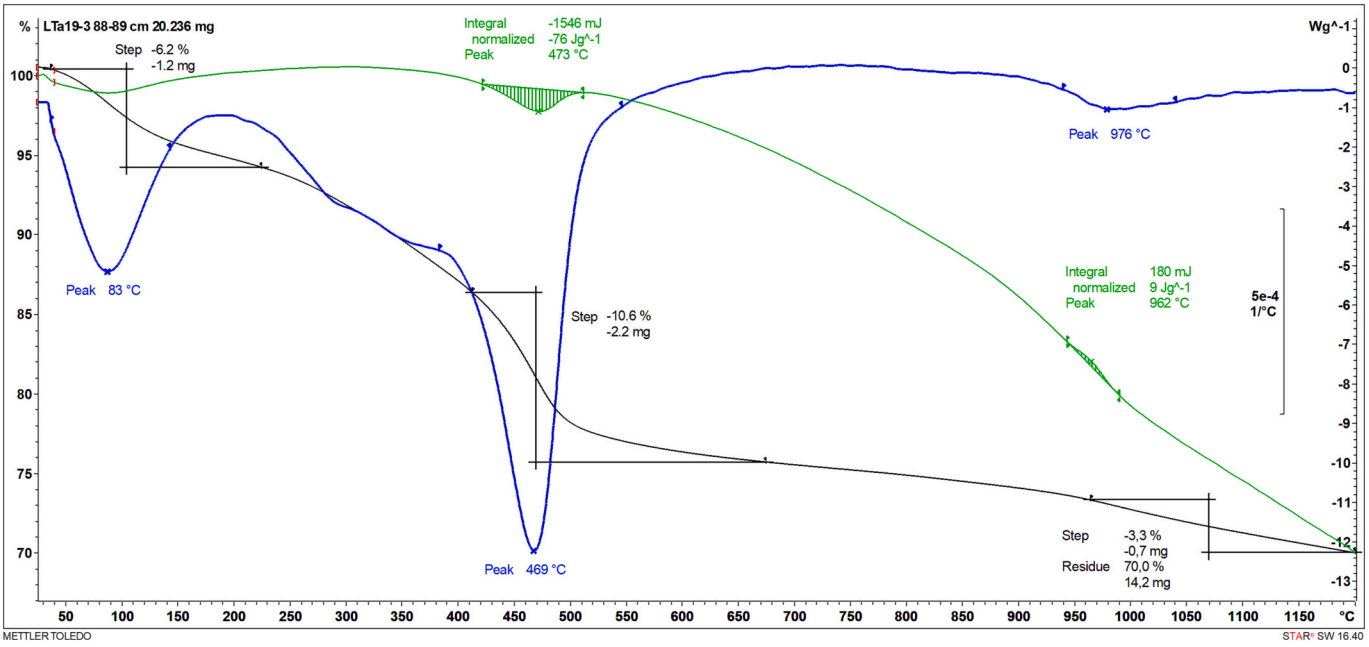

Fig. 3. STA curves of sample LTa19–3 88–89 cm that contains the highest abundance of kaolinite in the analyzed bulk sediments. TG, loss of weight (%): black curve, DSC: green curve, DTG: blue curve. (For interpretation of the references to colour in this figure legend, the reader is referred to the web version of this article.)

layers characterized by low SCOPIX levels corresponded to positive incursions in Ti but negative incursions in Br. Sediment organic carbon (C) and nitrogen (N) contents in LLEs19–2 followed a pattern similar to that of Br that may be associated with organic matter in lake sediments (Ziegler et al., 2008; Davies et al., 2015). The relative abundance of clay (<2 μm fraction) followed a reverse pattern. Similarly, an opposite pattern was observed for $\delta^{13}C$ that displayed the lowest (most ^{13}C-depleted) values during periods of elevated organic content and Br. C/N ratio and $\delta^{15}N$ in LLEs19–2 showed a gradual declining trend towards the sediment surface and, overall, a relatively small range of variability.

In LTa19-3, XRF elements and SCOPIX values showed similar coeval variation as in LLEs19–2 (Fig. 5). For example, a marked decrease in Ti counts observed between 58 and 62 cm corresponded to an increase in Br and SCOPIX values. Similarly, sediment C and N covaried with Br, and decreasing $\delta^{13}C$ values were generally associated with increasing organic content and Br. Clay (<2 μm fraction) abundance showed little variability in the lower part of the record (up to around 60 cm) whereon it followed a pattern somewhat similar to Ti. C/N values showed a gradual decline in the lower part of the core (~90–65 cm), with a distinct peak (>25) at around 60 cm. Sediment $\delta^{15}N$ values showed few trends aside from a step increase at around 60 cm.

For LTe19-4, Ti depicted an inverse trend with SCOPIX values and Br (Fig. 5), consistent with LLEs19–2 and LTa19-3. Compared to the other two lakes, the variations in LTe19-4 were generally more stable aside from a pronounced decrease in Ti in the lower part of the core, between ~104 and 94 cm, and a corresponding increase in Br. Sediment C and N data are not available for this section of the core but both indicators reflect higher organic content between ~90 and 75 cm, consistent with slightly elevated Br. An increasing trend in C and N, and to a lesser extent in Br, was also observed in the upper 20 cm of the core. As in LLEs19–2, clay (<2 μm fraction) abundance followed a pattern reverse to those observed in Br, C and N. Sediment $\delta^{13}C$ and C/N displayed distinctly low and high values, respectively, in the lower part of the core (i.e. ~75 cm downward), however, their variation was less clearly linked to variations in the XRF elements.

Regarding the RPCA, the first two PCs in core LLEs19–2 were sufficient to explain a cumulated variance of 74% (PC1 63%, PC2 11%). In the PC1-PC2 biplot diagram (Fig. S4), the elements were clustered into two main groups aligned along the PC1 axis (see the correlation matrix given in Fig. S4). Ti, Fe, Zr, Co, Sr and K (group 1) were aligned along the positive PC1 axis. Ni, Br and S associated with Si and Al (group 2) plotted along the negative PC1 axis. Ca varied along the positive PC2 axis. Pb and Mn were the less significant elements in the distribution, located in an intermediate position between PC1 and PC2.

In core LTa19-3, the elements were distributed in 3 groups and 69% of the variance was explained by 3 PCs (i.e. PC1 45%, PC2 14%, PC3 10%). The first two groups were aligned along the PC1 axis whereas group 3 was associated with the PC2 axis. Group 1 (Ti, Fe, Co, Zr, Mn and Pb but with a low contribution data in Fig. S4) was associated with negative PC1 axis values whereas group 2 (S and Br associated with Ni and Al) was distributed along the positive PC1 axis. Group 3 (Ca, Sr and K) was clustered along the PC2 axis.

The RPCA analysis on LTe19-4 revealed 4 significant PCs (i.e. PC1 31%, PC2 21%, PC3 15%, PC4 13%) with a cumulative variance of 80%. The elements were scattered in the PC1-PC2 binary plot. At least 4 groups of elements were evidenced, i.e., Ni, Sr and Br (group 1), Co, Fe and Zr (group 2), Ti, Si and K (group 3) and, Pb and Ca (group 4) whereas Al and Sr were not significant (correlation matrix given in Fig. S4).

4.4. Core chronology

In LLEs19–2, the $^{210}Pb_{xs}$ activity decreased from 288 mBq/g at 2.5 cm down to a negligible level at 16.5 cm, giving a low sediment accumulation rate of 0.09 cm/yr. For LTa19-3, the relatively constant $^{210}Pb_{xs}$ activity in the upper 5 cm suggested a mixed layer, which is consistent with the homogeneous texture underlined by the SCOPIX image (Fig. 2). Below this mixed layer, the decrease in ^{210}Pb excesses resulted in a sediment accumulation rate of 0.6 cm/yr. LTe19-4 presented a rather regular exponential decrease of $^{210}Pbxs$ reaching negligible activities at about 25 cm, resulting in an intermediate sediment accumulation rate of 0.255 cm/yr compared to the other two lakes.

The age models of the three cores (Fig. S5) were derived from the depth profiles of $^{210}Pb_{xs}$ in the upper 17, 23 and 61 cm of the sediment in cores LLEs19–2, LTe19-4 and LTa19-3, respectively. Assuming a surface age of AD2019 (i.e. coring year) and a constant sediment accumulation rate, LTa19-3 covers an interval of <160 yr whereas LLEs19–2 and LTe19-4 are well beyond the timescale of $^{210}Pb_{xs}$ with ~430 yr in LTe19-

4 and ≤ 600 yr in LLEs19–2. In terms of temporal resolution, only the sedimentation rate for LTa19-3 would allow a sufficient resolution to investigate pluriannual ENSO variability with a sampling resolution of 1 cm (i.e. 1 cm corresponds to 1.7 years for LTa19-3, 4 years for LTe19-4 and 11 years for LLEs19–2).

5. Discussion

5.1. Origin of minerals

In the three studied crater lakes, the mineralogical assemblages are composed of variable proportions of primary minerals, probably derived from the volcanic crater substrate by erosion and runoff and secondary minerals formed by weathering and pedogenetic processes in the upper soil cover and possibly by hydrothermal alteration. The volcanic-derived primary minerals are dominated by andesite (up to 54% in LLEs19–2), which may be associated with some forsterite, diopside and/or amphibole (Table S2).

Concerning the clay minerals, the origin of kaolinite is most probably multifold. First, kaolinite is a ubiquitous secondary mineral, whose abundance reaches 65% in LTe19-4 and up to 74% in LTa19-3, whereas it accounts for <45% in LLEs19–2 (Table S2). SEM observations (Fig. S3) confirmed that, at least, part of the kaolinite was formed by weathering of primary magmatic-derived plagioclase or Fe—Mg minerals. The presence of secondary kaolinite in the sediments of the three studied lakes probably reflects moderate hydrolysis conditions under tropical warm and humid conditions in the soils (e.g. Chamley, 1989) covering the internal crater flanks. Crater lakes represent small and closed sedimentary basins with a rapid source-to-sink transfer. Clay minerals in their sediments are useful indicators of paleoclimate conditions. However, pedogenesis is a slow process and the abundance of kaolinite observed in the crater lake sediments most likely reflects weathering conditions over the past millennia (Thiry, 2000).

Second, the broad reflection at 7.3 Å observed in the bulk XRD patterns of the Mexican lacustrine samples may indicate the presence of some halloysite-7 Å in addition to kaolinite. Halloysite-10 Å, renamed hydrohalloysite (Hatert et al., 2023), has been found in weathered or hydrothermally altered rocks, saprolites, and soils (Joussein et al., 2005). Hydrohalloysite is especially abundant in newly formed volcanic ash soils associated with quartz and cristobalite, formed by hydrothermal alteration of volcanic rocks at low temperatures (e.g., in New Zealand, Joussein et al., 2005). Such an origin is consistent with the volcanic substrate of the lakes studied and the presence of cristobalite. Sample preparation may explain the absence of hydrohalloysite in the crater lake samples, as hydrohalloysite can be quickly transformed into halloysite-7 Å under ambient temperature and humidity conditions or by heating ≥40 °C (Joussein et al., 2005). In addition, hydrohalloysite has been considered as an early weathering product in lateritic soils (Robert and Herbillon, 1990), representing an intermediate weathering stage between recent soil rich in allophane and more weathered soils rich in kaolinite and iron oxides in tropical and subtropical areas (Ndayiragije and Delvaux, 2004). The abundance of halloysite relative to kaolinite would decrease with increasing weathering stage (Joussein et al., 2005).

In Tacámbaro, the association of kaolinite with some diaspore, confirmed by SEM observation (Fig. S3), indicates complete leaching of silica under strong hydrolysis corresponding to an alitisation process. This process is indicative of stronger drainage that may occur along the steepest slope of the crater flank. The presence of both kaolinite and diaspore only in LTa19-3 emphasizes stronger chemical weathering conditions in the Lake Tacámbaro catchment.

Among the other minerals observed, the presence of carbonates in all samples of LLEs19–2, except in the dark layer at 14–15 cm (Fig. 2), reflects a biological component mainly associated with gastropod shells. In LTe19-4, some carbonates are detected by XRD. These carbonates are probably authigenic and related to the productivity of the lake as there are no carbonates in the watershed. Cristobalite is most probably related to the presence of volcanic glass. In addition, the abundance of cristobalite, especially in LTa19-3 (≤ 16%), could reflect the diatom productivity of the water column, as opal is an unstable amorphous silica mineral. The transition from amorphous opal-A to crystallized opal-CT (CT for cristobalite-tridymite) is a continuum controlled by a microscale dissolution-reprecipitation process in a near-surface environment (Jones and Renaut, 2007). Opal-A is progressively converted to opal-CT due to a decrease in d-spacing and porosity and an associated increase in density (Rice et al., 1995). Jones and Renaut (2007) emphasized that this process can be accelerated by the addition of Si from external sources. Indeed, such supply is supported in closed tropical crater lakes by silica-rich leachate solution delivered by monosialitisation and eventually alitisation processes.

5.2. Characterization of 1:1 layer

In the bulk powder XRD patterns the broad reflection at 7.3 Å reflects the presence of a poorly ordered kaolinite, most probably in association with some halloysite-7 Å. Halloysite-7 Å is characterized by a broad reflection at 7.3 Å, which is difficult to decipher with a poorly ordered kaolinite, particularly when they are mixed (Brindley, 1980a). A few percentages of hydrohalloysite (cif file obtained reported on Text S1b) were found, in addition to kaolinite, in the bulk and clay <2 μm fraction of at least one surface soil of the crater lake Teremendo (Fig. S6). In the following text, the term kaolinite is used sensu *lato* for a mixture of kaolinite and some halloysite-7 Å.

The thermogravimetric (TG) curves display two main mass losses characteristic of kaolinitic clays (Fig. 4). The first endothermic mass loss at 40–130 °C corresponds to the loss of adsorbed water. This pronounced endothermic reaction is consistent with the presence of both disordered kaolinite and halloysite-7 Å (Emmerich, 2010).

The second pronounced endothermic peak corresponds to the dehydroxylation of kaolinite/halloysite and its transformation in metakaolinite (e.g. Wang et al., 2011). The temperature of the reaction, as measured by DTG curves, is between 444 and 474 °C, whereas the dehydroxylation of kaolinite often occurs at higher temperatures between 530 and 630 °C (Emmerich, 2010). However, the measured dehydroxylation temperature is influenced by several factors, such as the mineral assemblage and, in particular, the abundance of kaolinite in the sample (Anand and Gilkes, 1987), the crystallinity of kaolinite (Földvári, 2011) but also the experimental conditions (Guggenheim and Van Groos, 2001; Heide and Földvari, 2006). Anand and Gilkes (1987) observed an increase in dehydroxylation temperature from 454 to 491 °C with increasing kaolinite abundance in soil samples. According to Földvári (2011), the position of the dehydroxylation peak was observed in lower temperature ranges for disordered kaolinites (530–570 °C) than for ordered kaolinites (570–630 °C). For the studied samples, there is no clear relationship between the abundance of kaolinite in the bulk sample (i.e. between 27 and 76%) and the dihydroxylation temperature. Therefore, the kaolinites studied most probably correspond to extremely disordered crystals (Smykatz, 1974), associated with some halloysite-7 Å.

A third mass loss of 3 to 5% occurring between 890 and 990 °C corresponds to a small exothermic peak associated with the crystallisation of mullite ($Al_2Si_2O_{13}$). Again, the observed lower temperature range for this reaction (usually 940–1000 °C) and the moderate heat exchange confirm the disordered character of kaolinite (Emmerich, 2010) and the presence of some halloysite-7 Å.

FTIR spectra (Fig. 4) confirms the poorly crystallized character of kaolinite. Well-ordered kaolinite is characterized by four absorption bands in the 3700–3600 cm^{-1} range associated with the stretching of OH-groups and by two absorption bands in the 1000–900 cm^{-1} range associated with the bending (Bich et al., 2009). However, the FTIR spectra from Tacámbaro and Teremendo samples display only two absorption bands between 3700 and 3620 cm^{-1} (i.e. at 3689–3699 and

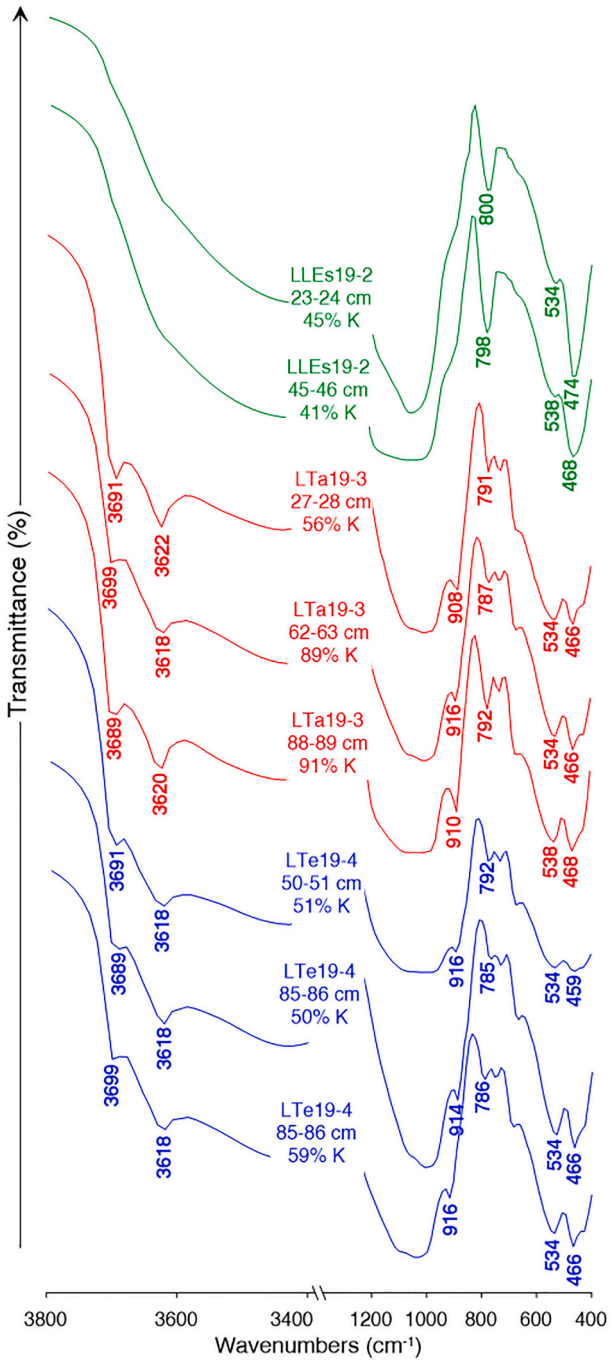

Fig. 4. Examples of FTIR curves on a selection of kaolinite-rich samples.

3618–3622 cm^{-1} - Fig. 4). The absence of vibration bands at 3670 and 3650 cm^{-1} indicates poorly order kaolinite (Vaculikova et al., 2011). It is also supported by the presence of only one absorption band identified in the 1000–900 cm^{-1} range (i.e. between 908 and 916 cm^{-1}) due to the OH deformation of inner hydroxyl group (Vaculikova et al., 2011). Note the peak near 540 cm^{-1} that coincides with Al-O-Si deformation in kaolinite (Madejová et al., 2010).

In addition to kaolinite, a mass loss (~5%) observed in the TG curve (Fig. 3) between the dehydratation and dehyhroxylation reactions reflects the presence of organic matter (Mackenzie, 1957) and hydrated phases such as opal in the bulk sediment. In the FTIR spectra (Fig. 4), the absorption bands at 794–796 and 467–474 cm^{-1} confirmed the presence of silica minerals (i.e., quartz and cristobalite in XRD patterns). Related to the Si-O-Si bending vibration, they usually grow from crystalline to non-crystalline varieties like opal A (Graetsch, 1994). The absence of absorption bands between 3090 and 3460 cm^{-1} confirms the absence of gibbsite and boehmite (Kloprogge et al., 2002), which were not detected by XRD. Note that the presence of diaspore, evidenced by SEM in LTa19-3 (Fig. S3), was not confirmed by FTIR (Frost et al., 1999).

5.3. *Significance of kaolinite variability in the sedimentary record*

Fig. 5 shows the parallel evolution of kaolinite in regard to the Br/Ti ratio, i.e. a ratio selected as a proxy for lake productivity (Agnihotri et al., 2008). The use of Br/Ti as a reliable proxy for lake productivity in the studied lakes is supported by the bulk organic matter geochemistry (Fig. 5). In all three lakes, the concomitant increases in sediment organic content (C and N) and Br/Ti were matched by generally low or declining $\delta^{13}C$ values, likely related to increased phytoplankton productivity (Meyers, 2003). Similar low $\delta^{13}C$ values may also be associated with terrestrial organic matter from C3 plants (typical values around −27‰) (Meyers, 1997), however, the opposite patterns for detrital elements (such as Ti) provide no evidence for increased catchment material fluxes. C/N values, often used to indicate relative changes in autochthonous and allochthonous organic matter inputs, showed few consistent changes but the generally low values point to a strong autochthonous component (Meyers, 2003) suggesting that the shifts in sediment C and N content (and thus Br/Ti) are tightly connected to primary production in the lake.

In LLEs19-2, the kaolinite abundance, which varies by a factor of 2 over the last 5 centuries follows a parallel trend with the Br/Ti ratio (Fig. 6). The highest kaolinite abundance ~~of~~ (i.e. 45% at 23–24 cm) corresponds to a high Br/Ti ratio. The LLEs19–2 record displays four distinct intervals with higher kaolinite abundance: ca. 1450, 1600, 1760–1820 and 1940–1980 CE.

In LTe19-4, the kaolinite abundance ranges from 41 to 65% over the last four centuries, with three intervals marked by higher kaolinite abundance at ~1640–1740, 1830–1900 and 1950–2019 CE. Although the range of variation is smaller than in LLEs19–2, the maximum abundance of kaolinite (i.e. 65% at 100–101 cm) also coincides with a pronounced positive excursion in the Br/Ti ratio around ca. 1650 CE. An increase in kaolinite is observed in the LLEs19–2 record within a similar time window (~1600 CE).

Due to a higher sedimentation rate, the core LTa19-3 covers only 160 years, allowing a high temporal resolution. In this short time period, the kaolinite profile (Fig. 6) displays a broad variation (37–74%) with higher values observed in two intervals, i.e. in the lower part of the record (1865–1875 CE) and between 1930 and 1985 CE. As in core LLEs19–2, and to some extent in LTe19-4, the kaolinite abundance follows the evolution of the Br/Ti ratio in the lower part of the record (93–55 cm, ~1860–1925 CE). It is hypothesized that the covariance between kaolinite abundance and the Br/Ti ratios reflects lake productivity and, by extension, natural variations in lake level. In spring, warmer temperatures favour high biological productivity and keep lake level low through evaporation. The onset of rainfall brings nutrients and detrital material, including kaolinite-rich clayey particles, into the lake. The sedimentation of kaolinite may then be related to its rapid adsorption on the abundant organic matter present in the water column (Guo et al., 2023) and to the settling of the organo-mineral aggregates due to their density. This is supported by the low abundance of clay-sized particles during organic-rich periods, particularly distinct in LLEs19–2 (Fig. 5).

There is no obvious relationship between the regional (Harris et al., 2020) or local temperature data (CONAGUA-SMN web platform, http://clicom-mex.cicese.mx) and the kaolinite profile in core LTa19-3. The lowest temperature interval recorded in the local meteorological data (1950–1990 CE) does not coincide with the lowest kaolinite abundance in LTa19-3. The sharp increase in kaolinite observed during 1925–1930 CE occurs during an interval of low regional temperatures but it is consistent with an increase in local precipitation.

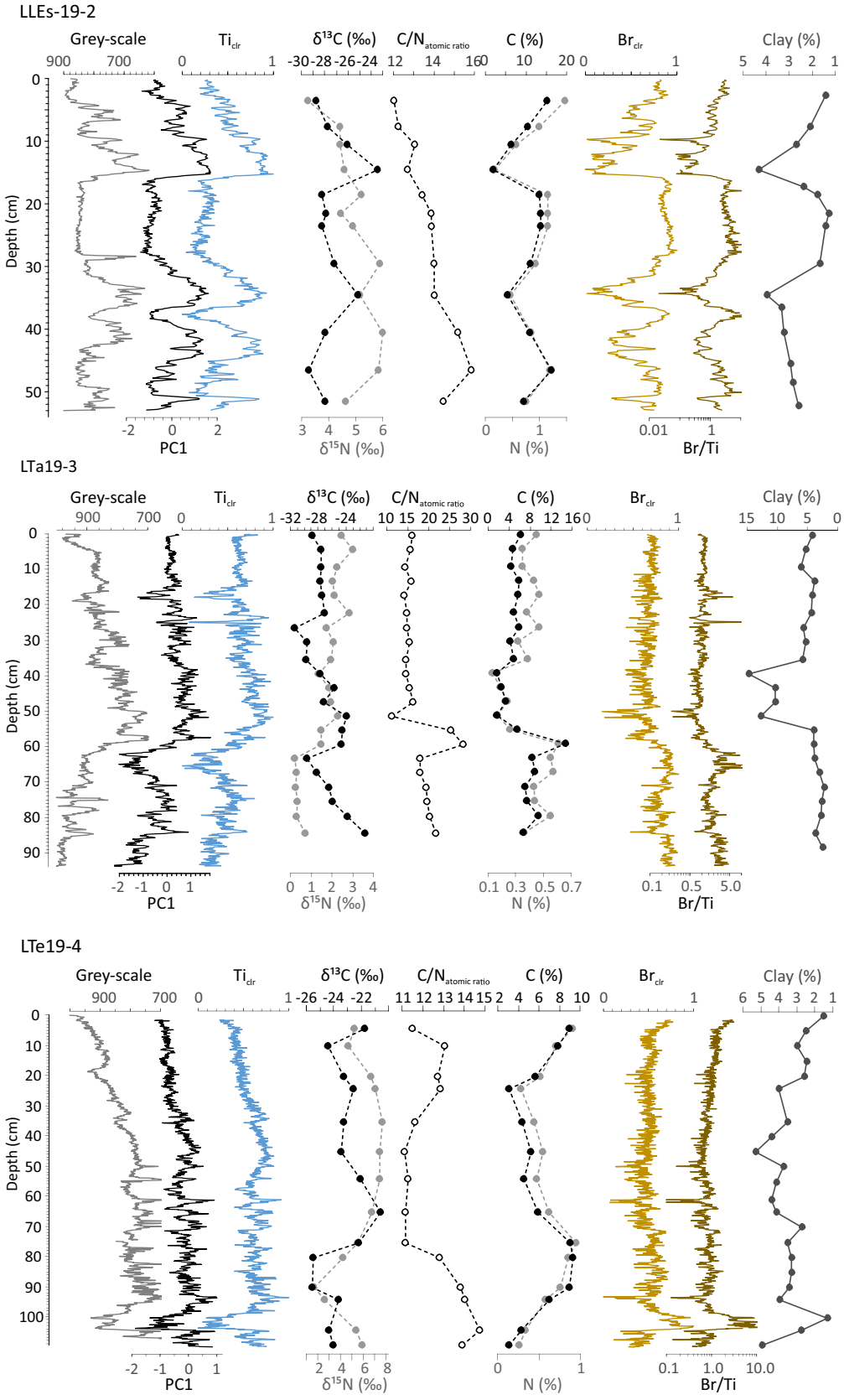

Fig. 5. Selection of clr transformed XRF element profiles (Ti_{clr}, Br_{clr}) and elemental ratio (Br/Ti) reported together with SCOPIX, PC1 score data, organic geochemistry (carbon [C] and nitrogen [N] concentrations and isotope ratios), and relative clay abundance (<2 μm fraction). Note the scale for SCOPIX values and clay abundance is inverted to present a parallel evolution of the profiles.

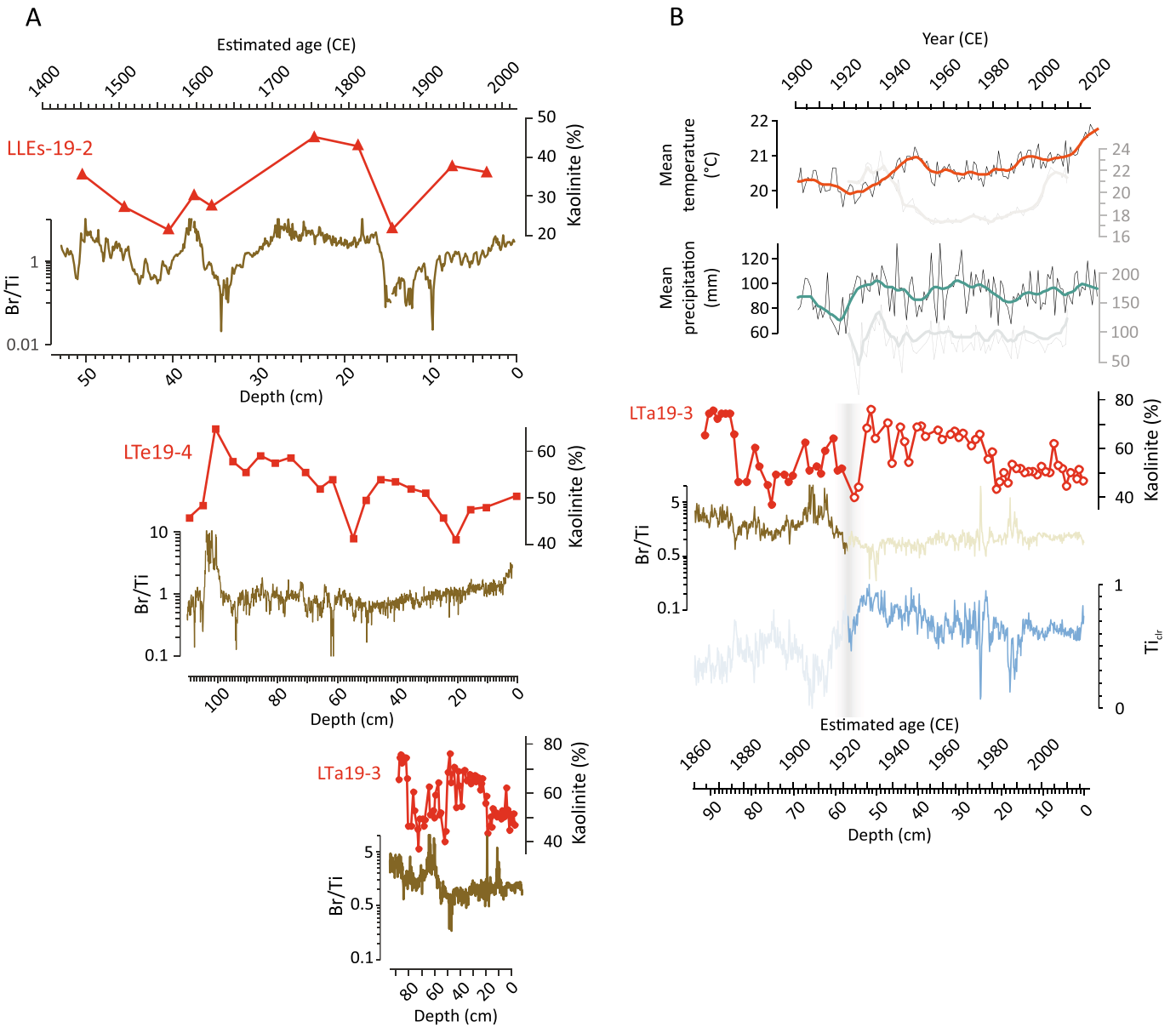

Fig. 6. Temporal evolution of relative kaolinite abundance, Ti and Br/Ti in the studied three sediment cores over the past centuries. Note that the age estimates, based on $^{210}Pb_{xs}$ data, are tentative beyond the past century. Comparison between temporal evolution of relative kaolinite abundance, Ti and Br/Ti in core LTa19-3 and regional and local temperature and precipitation trends over the past decades. Regional climate trends (indicated in colour) are based on the CRU TS (Climatic Research Unit gridded Time Series) dataset (CRU TS Version 4.06 - Harris et al., 2020) and local (indicated in grey) climate data derive from a nearby weather station (station Tacámbaro, 16,123) accessed through the CONAGUA-SMN web platform (http://clicom-mex.cicese.mx). The annual mean for precipitation is 1168 mm/yr for Tacámbaro, 896 mm/yr for Villa Jimenez station (nearby lake Los Espinos) and 700 mm/yr for Teremendo. Thickened lines depict lowess smooth curves (span 0.1). The presumed timing of the canal construction is indicated with a grey vertical bar.

In the upper section of core LTa19-3, there is no clear relationship between the Br/Ti ratio and kaolinite (Fig. 6). The kaolinite abundance varies rather in parallel with Ti, although the different resolution of the two proxies prevents a detailed comparison. This sharp change probably reflects a local disturbance around Lake Tacámbaro. Ortega-Guerrero et al. (2021) reported that the water level of Lake Tacámbaro was regulated by the construction of an artificial canal in the early 20th century. The exact date of this human intervention is unknown. The distinct peak in C/N values at around 60 cm (Fig. 5), coincident with the decoupling between kaolinite and Br/Ti ratio (Fig. 6), may well indicate a transient increase in catchment inputs associated with the construction work. After the construction of the canal, the sharp increase in kaolinite occurs during an interval of increased local rainfall. This change in local meteorological conditions (i.e. the sharpest change during the 20th century) probably enhances surface runoff, delivering more detrital elements and kaolinite to Lake Tacámbaro.

6. Conclusions

- Disordered kaolinite is the dominant secondary mineral present in all sediment samples from the 3 crater lakes investigated. This clay mineral is partly formed by moderate hydrolysis, a process consistent with the regional tropical warm and humid conditions of Central Mexico.
- The broad reflection at 7.3 Å observed in the bulk XRD patterns of the Mexican lacustrine samples underlines the presence of some halloysite-7 Å in addition to kaolinite. Halloysite is most probably formed by hydrothermal alteration of volcanic glasses.

- The presence of diaspore in Lake Tacámbaro probably reflects a more efficient local drainage along the steepest slope of the crater, resulting in complete removal of silica.
- Statistical treatment of the XRF core scanner data indicates an opposite relationship between detrital elements (Ti, K, Fe) and organic matter-related elements (Br, S, Ni).
- In lakes Los Espinos and Teremendo, the kaolinite abundance is the highest when the detrital flux (e.g. Ti) is the lowest and the organic matter flux is the highest. Kaolinite may be adsorbed onto the organic matter particles present in the water column and then settle to the lake bottom. Under natural conditions, the kaolinite abundance in the crater lake sediments may be a proxy for lake productivity and an indirect proxy for lake level (i.e. higher kaolinite abundance associated with lower lake level).
- For Lake Tacámbaro, the construction of a canal in the early 20th century to regulate the lake level suppresses the link between the kaolinite and lake productivity observed in the lower core section (pre-1925 CE). In the upper core section (i.e. post 1925 CE), kaolinite covaries with detrital elements such as Ti which are carried by surface runoff. The abundance of kaolinite is sensitive to rainfall intensity particularly when human intervention regulates lake levels.

CRediT authorship contribution statement

Nathalie Fagel: Conceptualization, Methodology, Formal analysis, Funding acquisition, Investigation, Project administration, Writing – original draft, Writing – review & editing, Supervision. **Isabel Israde-Alcantara:** Conceptualization, Funding acquisition, Investigation. **Reza Safaierad:** Data curation, Investigation, Writing – review & editing, Visualization. **Marttiina Rantala:** Software, Validation, Formal analysis, Visualization, Writing – review & editing. **Sabine Schmidt:** Formal analysis, Writing – review & editing, Visualization. **Gilles Lepoint:** Formal analysis. **Pierre Pellenard:** Formal analysis, Writing – review & editing. **Nadine Mattielli:** Conceptualization, Funding acquisition, Supervision, Project administration. **Sarah Metcalfe:** Conceptualization, Writing – review & editing.

Declaration of Competing Interest

The authors declare the following financial interests/personal relationships which may be considered as potential competing interests:

Fagel Nathalie reports financial support was provided by Fund for Scientific Research. Mattielli Nadine reports financial support was provided by Fund for Scientific Research.

Data availability

Data will be made available on request.

Acknowledgments

The fieldwork was done in June 2019 by N. Fagel and I. Israde-Alcantara, with the help of Luis Matilde Gacia, Julio Cañas, David Sanchez and Angel Zamudio. Thanks to Arturo Chacon for providing a boat location. Part of the analysis costs was supported by a FNRS funding for the PDR proposal HolMecl 2020-2025. The authors thank Joel Otten and Nicolas Delmelle (Geology, ULiège) for their technical support with the sedimentological and mineralogical preparations and analyses. Subsampling and sedimentological analyses were done as part of the master thesis of Gaelle Wanlin. Prof. Frédéric Boulvain (Sedimentology, ULiège) brought his expertise on sedimentological features and core description. Prof. Frédéric Hatert (Mineralogy, ULiège) helped with the TOPAS software. SEM-EDS observations were made with the support of Régis Parvaud, ARCEN analytical platform of the University of Burgundy (Dijon, France).

Appendix A. Supplementary data

Supplementary data to this article can be found online at https://doi.org/10.1016/j.clay.2023.107211.

References

Adrian, R., O'Reilly, C.M., Zagarese, H., Baines, S.B., Hessen, D.O., Keller, W., Livingstone, D.M., Sommaruga, R., Straile, D., Van Donk, E., 2009. Lakes as sentinels of climate change. Limnol. Oceanogr. 54, 2283–2297.
Agnihotri, R., Altabet, M.A., Herbert, T.D., Tierney, J.E., 2008. Subdecadally resolved paleoceanography of the Peru margin during the last two millennia. Geochem. Geophys. Geosyst. 9.
Alcocer, J., Escobar, E., Lugo, A., 2000. Water use (and abuse) and its effects on the crater-lakes of Valle de Santiago, Mexico. Lakes Reserv. Res. Manag. 5, 145–149.
Anand, R., Gilkes, R., 1987. An application of thermogravimetry to quantitative studies of feldspar alteration in soils. J. Therm. Anal. Calorim. 32, 1163–1175.
Appleby, P.G., Oldfield, F., 1978. The calculation of lead-210 dates assuming a constant rate of supply of unsupported 210Pb to the sediment. Catena 5, 1–8.
Barron, J.A., Metcalfe, S.E., Addison, J.A., 2012. Response of the North American monsoon to regional changes in ocean surface temperature. Paleoceanography 27.
Bartington-Instruments, 2008. OM0408 - Operation Manual for MS2 Magnetic Susceptibility System. Bartington Instruments Limited, Oxford, England.
Bich, C., Ambroise, J., Péra, J., 2009. Influence of degree of dehydroxylation on the pozzolanic activity of metakaolin. Appl. Clay Sci. 44, 194–200.
Bish, D.L., 1993a. Rietveld refinement of the kaolinite structure at 1.5 K. Clay Clay Miner. 41, 738–744.
Bish, D.L., 1993b. Studies of Clays and Clay Minerals Using X-Ray Powder Diffraction and the Rietveld Method. Los Alamos National Lab, NM (United States).
Bradbury, J.P., 2000. Limnologic history of Lago de Patzcuaro, Michoacan, Mexico for the past 48,000 years: impacts of climate and man. Palaeogeogr. Palaeoclimatol. Palaeoecol. 163, 69–95.
Briddon, C.L., Metcalfe, S., Taylor, D., Bannister, W., Cunanan, M., Santos-Borja, A.C., Papa, R.D., McGowan, S., 2023. Changing water quality and thermocline depth along an aquaculture gradient in six tropical crater lakes. Hydrobiologia 850, 283–299.
Brindley, G.W., 1980a. Order-disorder in the clay mineral structures. In: Brindley, G.W., Brown, G. (Eds.), Crystal Structures of Clay Minerals and their X-Ray Identification. Mineralogical Society, London, pp. 125–196.
Brindley, G.W., 1980b. Quantative analysis of clay mixtures. In: Brindley, G.W., Brown, G. (Eds.), Crystal Structures of Clay Minerals and their X-Ray Identification. Mineralogical Society, London, pp. 125–196.
Caballero, M., Vázquez, G., Ortega, B., Favila, M.E., Lozano-García, S., 2016. Responses to a warming trend and "El Niño" events in a tropical lake in western México. Aquat. Sci. 78, 591–604.
Candès, E.J., Li, X., Ma, Y., Wright, J., 2011. Robust principal component analysis? J. Assoc. Comput. Mach. 57, 1–37.
Castro, C.L., McKee, T.B., Pielke, R.A., 2001. The relationship of the North American monsoon to tropical and North Pacific Sea surface temperatures as revealed by observational analyses. J. Clim. 14, 4449–4473.
Chamley, H., 1989. Clay formation through weathering. Clay Sedimentol. 21–50.
Cifuentes, R.M.U., Fucugauchi, J.U., 1999. Paleomagnetic study of the Valle de Santiago volcanics, Michoacán-Guanajuato volcanic field, Mexico. Geofis. Int. 38, 217–230.
Cobb, K.M., Westphal, N., Sayani, H.R., Watson, J.T., Di Lorenzo, E., Cheng, H., Edwards, R., Charles, C.D., 2013. Highly variable El Niño–southern oscillation throughout the Holocene. Science 339, 67–70.
Davies, S.J., Lamb, H.F., Roberts, S.J., 2015. Micro-XRF core scanning in palaeolimnology: recent developments. In: Micro-XRF Studies of Sediment Cores: Applications of a Non-Destructive Tool for the Environmental Sciences, pp. 189–226.
Davis, J.C., 2002. Statistics and Data Analysis in Geology. Wiley & sons, New York.
Douglas, M.W., Maddox, R.A., Howard, K., Reyes, S., 1993. The mexican monsoon. J. Clim. 6, 1665–1677.
Drits, V., Besson, G., Muller, F., 1995. An improved model for structural transformations of heat-treated aluminous dioctahedral 2: 1 layer silicates. Clay Clay Miner. 43, 718–731.
Emmerich, K., 2010. Thermal Analysis in the Characterization and Processing of Industrial Minerals.
Fagel, N., Alvarez, D., Namur, O., Devidal, J.-L., Nuttin, L., Schmidt, S., Jana, P., Torrejon, F., Bertrand, S., Araneda, A., 2017. Lacustrine record of last millennia eruptions in Northern Chilean Patagonia (45–47° S). The Holocene 27, 1227–1251.
Ferrari, L., Orozco-Esquivel, T., Manea, V., Manea, M., 2012. The dynamic history of the Trans-Mexican Volcanic Belt and the Mexico subduction zone. Tectonophysics 522, 122–149.
Filzmoser, P., Fritz, H., Kalcher, K., 2018. pcaPP: Robust PCA by Projection Pursuit. R Foundation for Statistical Computing, Vienna, Austria.
Földvári, M., 2011. Handbook of Thermogravimetric System of Minerals and its Use in Geological Practice. Geological Institute of Hungary Budapest.
Frost, R.L., Kloprogge, J.T., Russell, S.C., Szetu, J., 1999. Dehydroxylation and the vibrational spectroscopy of aluminum (oxo) hydroxides using infrared emission spectroscopy. Part III: diaspore. Appl. Spectrosc. 53, 829–835.
Frugone-Álvarez, M., Latorre, C., Giralt, S., Polanco-Martínez, J., Bernárdez, P., Oliva-Urcia, B., Maldonado, A., Carrevedo, M.L., Moreno, A., Delgado Huertas, A., 2017. A 7000-year high-resolution lake sediment record from coastal Central Chile (Lago

Vichuquén, 34° S): implications for past sea level and environmental variability. J. Quat. Sci. 32, 830–844.
Garrett, R.G., Garrett, M.R.G., 2018. Package 'rgr'. Appl Geochemistry EDA.
Gomez-Tagle Chavez, A., Bernal-Brooks, F., Alcocer, J., 2002. Sensitivity of Mexican water bodies to regional climatic change: three study alternatives applied to remote sensed data of Lake Patzcuaro. Hydrobiologia 467, 169–176.
Graetsch, H., 1994. Structural characteristics of opaline and microcrystalline silica minerals. Rev. Mineral. Geochem. 29, 209–232.
Guggenheim, S., Van Groos, A.K., 2001. Baseline studies of the clay minerals society source clays: thermal analysis. Clay Clay Miner. 49, 433–443.
Guilbaud, M.-N., Siebe, C., Layer, P., Salinas, S., 2012. Reconstruction of the volcanic history of the Tacámbaro-Puruarán area (Michoacán, México) reveals high frequency of Holocene monogenetic eruptions. Bull. Volcanol. 74, 1187–1211.
Guo, C., Guo, L., Bass, S., Manning, A.J., Jin, Z., Zhou, Y., 2023. On the role of organic matter composition in fresh-water kaolinite flocculation. J. Environ. Manag. 345, 118576.
Harris, I., Osborn, T.J., Jones, P., Lister, D., 2020. Version 4 of the CRU TS monthly high-resolution gridded multivariate climate dataset. Sci. data 7, 109.
Hasenaka, T., Carmichael, I.S.E., 1985. The cinder cones of Michoacan-Guanajuato, Central Mexico: their age, volume and distribution, and magma discharge rate. J. Volcanol. Geotherm. Res. 25, 105–124.
Hatert, F., Mills, S.J., Pasero, M., Miyawaki, R., Bosi, F., 2023. CNMNC guidelines for the nomenclature of polymorphs and polysomes. Mineral. Mag. 87, 225–232.
Heide, K., Földvari, M., 2006. High temperature mass spectrometric gas-release studies of kaolinite Al2 [Si2O5 (OH) 4] decomposition. Thermochim. Acta 446, 106–112.
Hemminger, W.F., Cammenga, H.K., 1989. Methoden Des Thermischen Analyse. Springer, Berlin.
Hernández-Morales, R., 2011. Fitoplancton de los lagos cráter de Michoacán, México.
Hernández-Morales, R., Ortega, M., Sánchez, J., Alvarado, R., Aguilera, M., 2011. Distribución estacional del fitoplancton en un lago cálido monomíctico en Michoacán, México. Biológicas Revista de la DES Ciencias Biológico Agropecuarias Universidad Michoacana de San Nicolás de Hidalgo 13, 21–28.
Higgins, R.W., Chen, Y., Douglas, A.V., 1999. Interannual variability of the North American warm season precipitation regime. J. Clim. 12, 653–680.
Holmes, J.A., Metcalfe, S.E., Jones, H.L., Marshall, J.D., 2016. Climatic variability over the last 30 000 years recorded in La Piscina de Yuriria, a Central Mexican crater lake. J. Quat. Sci. 31, 310–324.
Jones, B., Renaut, R.W., 2007. Microstructural changes accompanying the opal-A to opal-CT transition: New evidence from the siliceous sinters of Geysir, Haukadalur, Iceland. Sedimentology 54, 921–948.
Joussein, E., Petit, S., Churchman, J., Theng, B., Righi, D., Delvaux, B., 2005. Halloysite clay minerals—a review. Clay Miner. 40, 383–426.
Kienel, U., Bowen, S.W., Byrne, R., Park, J., Böhnel, H., Dulski, P., Luhr, J.F., Siebert, L., Haug, G.H., Negendank, J.F., 2009. First lacustrine varve chronologies from Mexico: impact of droughts, ENSO and human activity since AD 1840 as recorded in maar sediments from Valle de Santiago. J. Paleolimnol. 42, 587–609.
Kloprogge, J.T., Ruan, H.D., Frost, R.L., 2002. Thermal decomposition of bauxite minerals: infrared emission spectroscopy of gibbsite, boehmite and diaspore. J. Mater. Sci. 37, 1121–1129.
Lind, O.T., Doyle, R., Vodopich, D.S., Trotter, B.G., Limón, J.G., Dcivalos-Lind, L., 1992. Clay turbidity: Regulation of phytoplankton production in a large, nutrient-rich tropical lake. Limnol. Oceanogr. 37, 549–565.
Lorentz, B., Shanahan, N., Stetsko, Y.P., Zayed, A., 2018. Characterization of Florida kaolin clays using multiple-technique approach. Appl. Clay Sci. 161, 326–333.
Mackenzie, R.C., 1957. The Differential Thermal Investigation of Clays.
Madejová, J., Balan, E., Petit, S., 2010. Application of Vibrational Spectroscopy to the Characterization of Phyllosilicates and Other Industrial Minerals.
McPhaden, M.J., Zebiak, S.E., Glantz, M.H., 2006. ENSO as an integrating concept in earth science. science 314, 1740–1745.
Meyers, P.A., 1997. Organic geochemical proxies of paleoceanographic, paleolimnologic, and paleoclimatic processes. Org. Geochem. 27, 213–250.
Meyers, P.A., 2003. Applications of organic geochemistry to paleolimnological reconstructions: a summary of examples from the Laurentian Great Lakes. Org. Geochem. 34, 261–289.
Migeon, S., Weber, O., Faugeres, J.-C., Saint-Paul, J., 1998. SCOPIX: a new X-ray imaging system for core analysis. Geo-Mar. Lett. 18, 251–255.
Moore, D.M., Reynolds, R.C., 1989. X-Ray Diffraction and the Identification and Analysis of Clay Minerals. Oxford university press, Oxford.
Morales, R.H., Murillo, M.O., Villanueva, R.A., Heredia, J.S., Zarco, F.M., 2008. Variación anual del fitoplancton en el lago cráter La Alberca de Tacámbaro, Michoacán, México. In: Biológicas Revista de la DES Ciencias Biológico Agropecuarias Universidad Michoacana de San Nicolás de Hidalgo, 10, pp. 5–17.
Munsell, C., 1975. Munsell Soil Color Charts: Munsell Color. Baltimore, Maryland.
Ndayiragije, S., Delvaux, B., 2004. Selective sorption of potassium in a weathering sequence of volcanic ash soils from Guadeloupe, French West Indies. Catena 56, 185–198.
Ortega-Guerrero, B., Caballero, M., Israde-AlcáNtara, I., 2021. The Holocene record of Alberca de Tacámbaro, a tropical lake in western Mexico: evidence of orbital and millennial-scale climatic variability. J. Quat. Sci. 36, 649–663.
Park, J., Byrne, R., Böhnel, H., 2019. Late Holocene climate change in Central Mexico and the decline of Teotihuacan. Ann. Am. Assoc. Geogr. 109, 104–120.
Patterson, E., Swaffield, R., 1987. Thermal analysis. In: W, M.J. (Ed.), Handbook of Determinative Methods in Clay Mineralogy. Blackie and Son Limited, Glasgow, UK, pp. 99–132.
Pedro, G., 1968. Distribution des principaux types d'altération chimique à la surface du globe. Présentation d'une esquisse géographique. Rev. Géogr. Phys. Géol. Dyn. 2, 5.
R Development Core Team, R, 2013. R: A Language and Environment for Statistical Computing.
Rice, S., Freund, H., Huang, W., Clouse, J., Isaacs, C., 1995. Application of Fourier transform infrared spectroscopy to silica diagenesis; the opal-a to opal-CT transformation. J. Sediment. Res. 65, 639–647.
Rietveld, H., 1967. Line profiles of neutron powder-diffraction peaks for structure refinement. Acta Crystallogr. 22, 151–152.
Robert, M., Herbillon, A., 1990. Application aux argiles de sols. Genèse, nature et rôle des constituants argileux dans les principaux types de sols des environnements volcaniques insulaires, Matériaux argileux. Struct. Prop. Appl. 539–576.
Saalfeld, H., Wedde, M., 1974. Refinement of the crystal structure of gibbsite, A1 (OH) 3. Zeitschrift für Kristallographie-Crystalline Materials 139, 129–135.
Siebe, C., Guilbaud, M., Salinas, S., Chedeville-Monzo, C., 2012. Eruption of Alberca de los Espinos tuff cone causes transgression of Zacapu lake ca. In: 25,000 yr BP in Michoacán, México, IAS 4IMC Conference, Auckland, New Zeland, pp. 74–75.
Sigala, I., Caballero, M., Correa-Metrio, A., Lozano-García, S., Vázquez, G., Pérez, L., Zawisza, E., 2017. Basic limnology of 30 continental waterbodies of the Transmexican Volcanic Belt across climatic and environmental gradients. Bol. Soc. Geol. Mex. 69, 313–370.
Singer, A., 1984. The paleoclimatic interpretation of clay minerals in sediments—a review. Earth Sci. Rev. 21, 251–293.
Smykatz, K., 1974. The Determination of the Degree of (Dis-) Order of Kaolinites by Means of Differential Thermal Analysis.
Soria-Caballero, D.C., Garduño-Monroy, V.H., Alcalá, M., Velázquez-Bucio, M.M., Grassi, L., 2019. Evidence for quaternary seismic activity of the La Alberca-Teremendo fault, Morelia region, Trans-Mexican Volcanic Belt. Rev. Mexicana Ciencias Geol. 36, 242–258.
Środoń, J., 2002. Quantitative mineralogy of sedimentary rocks with emphasis on clays and with applications to K-Ar dating. Mineral. Mag. 66, 677–687.
Thiry, M., 2000. Palaeoclimatic interpretation of clay minerals in marine deposits: an outlook from the continental origin. Earth Sci. Rev. 49, 201–221.
Vaculikova, L., Plevova, E., Vallova, S., Koutnik, I., 2011. Characterization and Differentiation of Kaolinites from Selected Czech Deposits Using Infrared Spectroscopy and Differential Thermal Analysis.
Wang, H., Li, C., Peng, Z., Zhang, S., 2011. Characterization and thermal behavior of kaolin. J. Therm. Anal. Calorim. 105, 157–160.
Warr, L.N., 2022. Earth's clay mineral inventory and its climate interaction: a quantitative assessment. Earth Sci. Rev. 104198.
Weaver, C.E., 1989. Clays, Muds, and Shales. Elsevier.
Winder, M., Reuter, J.E., Schladow, S.G., 2009. Lake warming favours small-sized planktonic diatom species. Proc. R. Soc. B Biol. Sci. 276, 427–435.
Wogau, K.H., Arz, H.W., Böhnel, H.N., Nowaczyk, N.R., Park, J., 2019. High resolution paleoclimate and paleoenvironmental reconstruction in the Northern Mesoamerican Frontier for Prehistory to Historical times. Quat. Sci. Rev. 226, 106001.
Żarczyński, M., Wacnik, A., Tylmann, W., 2019. Tracing lake mixing and oxygenation regime using the Fe/Mn ratio in varved sediments: 2000 year-long record of human-induced changes from Lake Żabińskie (NE Poland). Sci. Total Environ. 657, 585–596.
Ziegler, M., Jilbert, T., de Lange, G.J., Lourens, L.J., Reichart, G.J., 2008. Bromine counts from XRF scanning as an estimate of the marine organic carbon content of sediment cores. Geochem. Geophys. Geosyst. 9.